

# Cytoskeletal and motility changes in human umbilical cord MSCs associated with nuclear-cytoplasmic RhoA redistribution during replicative senescence

Danila Bobkov<sup>1\*</sup> | Anastasia Polyanskaya<sup>2†</sup> | Anastasia Musorina<sup>1\*</sup> | Ekaterina Lomert<sup>1\*</sup> | Sergey Shabelnikov<sup>1\*</sup> | Galina Poljanskaya<sup>1\*</sup>

<sup>1</sup>Institute of Cytology of the Russian Academy of Science, 194064 Tikhoretsky ave. 4, St-Petersburg, Russia

<sup>2</sup>Peter the Great St. Petersburg Polytechnic University, Polytechnicheskaya, 29, St.Petersburg, 195251, Russia

## Correspondence

Tikhoretsky ave. 4, St-Petersburg, 194064, Russia  
Email: bobkov@incras.ru

## Present address

<sup>†</sup>Peter the Great St. Petersburg Polytechnic University, Polytechnicheskaya, 29, St.Petersburg, 195251, Russia

## Funding information

This article was published with the financial support from the Institute of Cytology RAS Director's Fund

Here we provide evidence for changes in cell motility and organization of the contractile apparatus of human umbilical cord MSCs in the process of replicative senescence. The colocalization dynamics of myosin-9,  $\alpha$ -actinin-4, and RhoA with F-actin and nuclei were examined in MSCWJ-1. Result shows that RhoA nuclear-cytoplasmic redistribution occurs during replicative senescence, with maximal RhoA/nucleus colocalization at passage 15. At the same time point, a decrease in myosin-9 and  $\alpha$ -actinin-4 colocalization with F-actin was found, and myosin-9 was found in cytosolic extracts in the assembly-incompetent form. Using the automated system of intravital confocal cytometry we found that changes in cytoskeleton organization correlates with cell motility characteristics in MSCWJ-1. Quantitative analysis of MSCWJ-1 movements revealed decline in cell speed from 9 to 36 passage. Results of cytoskeleton structural

**Abbreviations:** DMEM, Dulbecco's modified Eagle's medium; DOX, sodium deoxycholate; FBS, fetus bovine serum; FPLC, fast performance liquid chromatography; HRP, Horseradish Peroxidase; MSCs, mesenchymal stem cells; RCF, relative centrifugal force; PCA, principal component analysis; MSCWJ-1, human umbilical cord MSCs cell line; MW, molecular weight; bTau,  $\tau$ -Kendall rank correlation coefficient; Rs, Spearman's R correlation coefficient; tM, Manders correlation coefficient; Rval, Pearson correlation coefficient; SD, standard deviation

analysis together with cell motility characteristics allows us to divide the process of replicative senescence into two stages. The first stage lasts from thawing to passage 15 and is characterized by the accumulation of actin-binding proteins in the assembly-incompetent forms, nuclear RhoA accumulation and increase in movement tortuosity. The second stage lasts at passages 15 to 36 and characterized by an increase in the structural integrity of the actin cytoskeleton, exit of RhoA and  $\alpha$ -actinin-4 from nucleus and decrease in path tortuosity.

#### KEYWORDS

mesenchymal stem cells, *cellular senescence*, actin cytoskeleton, myosin-9,  $\alpha$ -actinin-4, RhoA, cell motility

## 1 | INTRODUCTION

At present, the urgent task of cell biology is the isolation and comparative characterization of human MSCs isolated from various sources. The importance of such studies stems from the features of the interaction of MSCs isolated from different tissues, with their characteristic microenvironment. The source of the MSC can determine their functional characteristics. Analysis of the characteristics that are decisive in maintaining the status of MSCs, as well as a number of other characteristics responsible for the most important cellular processes, contributes to the deepening of basic knowledge of human MSCs, which is important both for understanding the mechanisms of biological processes in the cell and for expanding opportunities for using MSCs in regenerative medicine. Due to the importance of MSCs for the functioning of the body, the mechanisms of MSC interaction with damaged tissues and organs are widely studied. It has been shown that one of the most important mechanisms of action of various MSCs on damaged tissues is their ability to migrate to these sites and exert a trophic action due to the secretion of bioactive factors that alter the microenvironment of damaged cells and, thereby, improving tissue repair. At present, the mechanisms of tissue repair using MSCs related to the production of cytokines and paracrine factors are widely discussed in the literature (Phinney and Prockop (2007); Carvalho et al. (2011); Guiducci et al. (2011); Gruenloh et al. (2011); Huang et al. (2013); Luo et al. (2013); Ando et al. (2014); Hendijani et al. (2015b); Hendijani et al. (2015a); Danieli et al. (2016); Julianto and Rindastuti (2016); Teixeira et al. (2017); Vulcano et al. (2016); Zachar et al. (2016)).

Non-immortalized cell lines undergo a process of replicative senescence. Replicative senescence is a complex process that can begin at the early passages and gradually increase in the process of long-term cultivation. It is characterized by a significant decrease or cessation of proliferation, shortening of telomeres, morphological changes, increased  $\beta$ -galactosidase activity, increased expression of the tumor suppressor genes, decreased DNA repair and antioxidant activity of senescence cells, due to reduced expression of the corresponding genes, a number of epigenetic changes (Wagner et al. (2008); Kuilman et al. (2010); Redaelli et al. (2012); Estrada et al. (2013); Savickienė et al. (2016); Danisovic et al. (2017); Koltsova et al. (2018); Alessio et al. (2018); Krylova et al. (2018); Niedernhofer et al. (2018); Truong et al. (2018); Yu et al. (2018)). It is important to emphasize that senescence of MSCs may be associated not only with replicative senescence, which can be traced during long-term cultivation of MSCs in vitro, but also with

factors external to MSCs. Senescence mechanisms affect both MSCs and microenvironment. In this regard, it is the interaction of MSCs and the microenvironment that ensures the age characteristics of MSCs. One of the essential signs of replicative senescence is a decrease in cell motility or cell migration. Violation of migration processes contributes to the deterioration of tissue repair (Geißler et al. (2012); Bertolo et al. (2015); Turinetto et al. (2016); Zhang et al. (2018)). Therefore, to use MSCs in regenerative medicine, it is necessary to know the nature of the process of replicative senescence in a particular line.

In order to find out how cellular senescence can interfere with use of cells in biomedical work, it is important to find out to what extent cell mobility is impaired during long-term cultivation. Cell migration occurs through close contact with the extracellular matrix, on which cells are spread, and depends on the organization of the actin cytoskeleton. In this regard, it is essential to study the role of senescence in the organization of the cytoskeleton. Actin cytoskeleton, including motor proteins, such as nonmuscle myosin isoforms, provide the driving forces for creating morphological diversity and the dynamics of mammalian cells (Vasiliev (1991), Omelchenko et al. (2002)). Currently, studies on the effect of replicative senescence on cytoskeleton reorganization are at the stage of accumulation of experimental results. There are a number of works describing molecular mechanisms and functional changes during the reorganization of the cytoskeleton during replicative senescence in different human and animal cell types (Larsen et al. (2003); Le Clainche and Carlier (2008); Wang and Jang (2009); Geißler et al. (2012); Özcan et al. (2016); Turinetto et al. (2016); Moujaber et al. (2019)). It is of considerable interest to analyze the effect of replicative senescence on cell motility and the reorganization of the actin cytoskeleton in the human MSC line, which has not been used in detail in such studies.

In this work, we used MSCWJ-1 cells that were not previously investigated. Little is known about how the structural aspects of these cells are modified as a result of replicative senescence. Thus, the objective of this study is analysis of replicative senescence in the process of long-term cultivation of the MSCWJ-1 in connection with the actin cytoskeleton state and the behavior of moving cells. To analyze the changes in actin cytoskeleton, we focused on two structural and one regulatory actin-binding proteins: myosin-9,  $\alpha$ -actinin-4, and small GTPase RhoA. Using immunofluorescence, liquid chromatography, and confocal microscopy-based quantitative image cytometry techniques, we investigated changes caused by replicative senescence in cell motility.

## 2 | RESULTS

### 2.1 | $\beta$ -Galactosidase activity

During long-term cultivation (passages 7–36) within each passage, the culture was filled by homogeneous cell populations of fibroblast-like cells. The results of  $\beta$ -galactosidase enzyme activity test shown in the table 1. The proportion of stained cells naturally increases with passage number, which confirms the senescent status of MSCWJ-1.

### 2.2 | Colocalization analysis

In order to follow the dynamics of the reorganization of the contractile apparatus during replicative senescence, we used the immunofluorescence method. Using polyclonal antibodies against myosin-9, we performed initial passage screening to identify features associated with replicative senescence. Assuming that the cells in the neighboring passages are negligibly little different from each other, we fixed MSCWJ-1 and analyzed the myosin-9/F-actin colocalization at passages: 7, 9, 12, 15, 18, 21, 25, 27, 28, 35, 36. First of all, it should be noted that in all examined passages, myosin-9 forms a characteristic striated pattern in the cells, represented by parallel bands that are perpen-

dicular to nearby stress fibrils. An example of such a striated pattern can be seen in Fig. 4C. In addition to the striated pattern, myosin-9 was detected in lamellae as separate spots (Fig. 4B). An increased number of cells with such spots was detected in preparations fixed at passages 15–20.

The results of colocalization analysis shown in the Fig. 1B. Myosin-9/F-actin colocalization decreases from high to moderate level during cultivation and reaches a minimum at passage 15. Then, the colocalization rises to a very high level at passage 28, after which it again decreases during passage of cultivation to passage 36, which was our last time point. The use of post hoc analysis revealed the most significant differences between groups associated with a decrease in colocalization at 15 and 18 passages (Fig 1C). For further research, we decided that 9, 15, 28, and 36 passages would be key points.

The immunofluorescence confocal images of WJMSC- 1 stained for  $\alpha$ -actinin-4 at passages 9, 15, 36 shown in Fig. 2.  $\alpha$ -Actinin-4 as well as myosin-9 was detected in cells at passages 9 and 36 in the form of striated patterns, less pronounced than in myosin-9, but nevertheless quite distinguishable. At passages 15–18  $\alpha$ -actinin-4 was detected also as spotted pattern and in focal adhesions. We studied the  $\alpha$ -actinin-4/F-actin and  $\alpha$ -actinin-4/Hoechst33342 colocalization at passages 7–36. The results are shown in Figure 2 (C),  $\alpha$ -actinin-4/Hoechst33342 colocalization decreases from moderate level to weak when moving from 28 to 36 passages. The same decrease is observed in the transition from 9 to 15 passage in case of  $\alpha$ -actinin-4/F-actin colocalization.

RhoA was detected in the nucleus, along the stress-fibers, in the perinuclear region, diffusely in the cytoplasm at passages 9–15 (Fig. 3). RhoA was detected mainly in the nucleus, along the stress-fibers, diffusely in the cytoplasm and in lamellipodias at passage 28–36. The colocalization of small GTPase RhoA with nuclei significantly increases from moderate to noticeable level while passage gone from 9 to 15, then decreases to the initial level at passage 28, and even more decreases to the weak level at passage 36. It should be noted that in almost half of the cells, the coefficient takes negative values, which indicates the complete absence of colocalization.

For a more detailed study of nuclear-cytoplasmic RhoA shuttle, we used the analysis of 3D models of nuclear regions based on confocal Z-stacks. At the passage 9, RhoA is distributed partly in the nucleus and partly in the cytoplasm, at the 15th passage for the most part inside the nucleus and in the perinuclear region, and at the 36th passage only along stress fibrils and in the cytoplasm (Fig. 4).

## 2.3 | Cell movement trajectory analysis

The results of quantitative analysis of 24h MSCWJ-1 cell movement tracks demonstrate statistically significant difference in almost all investigated parameters when comparing passages 9, 15, 36 (Fig. 5). The data obtained after tracks extraction were checked for normality using Shapiro-Wilk normality test, and it turned out that in the observation groups, all distributions are far from normal (see Supplementary for details, Table 7 and Fig. 2S). Therefore, to identify significant differences, we used the nonparametric Wilcoxon test. In the following comparisons differences are statistically insignificant: distance when comparing passage 15 to 36, and straightness when comparing passage 9 to 15. Speed and path length decreased with increase in passage number. The straightness of the trajectory increases with the passage from passage 15 to 36. The tortuosity of the trajectory increases with the transition from passage 9 to 15 and then decreases by passage 36 to a level significantly lower than it was at passage 9. The numerical values obtained from the analysis are shown in the table 2.

## 2.4 | Gel chromatography

Cytosolic extracts from WJMSC-1 were obtained in such a way that after centrifugation, nuclei, cell organelles, vesicles, and the cytoskeleton concentrated in the sediment. Supernatants were applied to a column calibrated using a set of proteins with known molecular weights. The range of fractions collection was chosen by us in such a way as to capture an area from 10 to 2000 kDa, this range was divided into 14 equal fractions (Fig. 6B). Comparison of elution profiles recorded during gel chromatographic separation of cell extracts at passages 9, 15, 36 reveals general similarity (Fig. 6A).

To investigate myosin-9 distribution among the fractions, membranes were stained with polyclonal antibodies against synthetic peptide corresponding to amino acids 1949–1960 of human nonmuscle myosin IIA and HRP-conjugated secondary anti-rabbit antibodies. Myosin-9 was detected at passage 9 in high molecular weight fractions 3–4 (approximately 1000–1500 kDa), and to a lesser extent in fraction 7 (correspondent to the size of the dimer 450 kDa), and in fraction 9, which is approximately equal to the size of the monomer 225 kDa. At passage 15, myosin-9 was detected mainly in fractions 3–4, with additional band above the main isoform. At passage 28, myosin-9 was detected at a high level in fractions 3–4, at a moderate level in fractions 5–9 (Fig. 6C).

To investigate  $\alpha$ -actinin-4 distribution among the fractions, membranes were stained with polyclonal antibodies against human  $\alpha$ -actinin-4 and HRP-conjugated secondary anti-rabbit antibodies.  $\alpha$ -Actinin-4 was detected as one peak eluted in fraction 6 (approximately 700 kDa) at all investigated passages (Fig. 6C).

To investigate  $\beta$ -actin distribution among the fractions, membranes were stained with mouse monoclonal anti- $\beta$ -actin antibodies and HRP-conjugated secondary anti-mouse antibodies.  $\beta$ -Actin is detected mainly in the 10–11 fractions at passage 9, correspondent to 45 kDa actin monomer. But at 15 and 28 passages  $\beta$ -actin also revealed in fractions 6–7 (approximately 500–100 kDa).

To investigate RhoA distribution among the fractions, membranes were stained with polyclonal antibodies against synthetic peptide corresponding to amino acids 177–189 located near the C-terminus of human RhoA and HRP-conjugated secondary anti-rabbit antibodies. At passage 9, RhoA was detected in fractions 6–10 as 100 kDa band, in fractions 6–7 as bands with approximately 50, 70, 80 kDa. At passage 15, RhoA was detected in fractions 6–10 as 100 kDa band, in fractions 6–8 as three band pattern (approximately 70, 80, 100 kDa). At passage 28, RhoA was detected in fraction 6 as two bands with MW approximately 70, 80 kDa. One band with a molecular weight of 21 kD was detected in passage 15 in fraction 3.

## 3 | DISCUSSION

Although a considerable amount of information is collected regarding replicative senescence since discovery that human cells cannot endlessly divide (Hayflick and Moorhead (1961)), little is known about the mechanisms of senescence in context of actin cytoskeleton structure and cell motility. Previous studies on MSCWJ-1 showed that already at passage 13, in addition to increasing  $\beta$ -galactosidase activity, the average doubling time in cell population also increases. At passage 28, in addition to above mentioned, other senescence signs also appear, such as changes in cell morphology, and a proliferation index decreases (Koltsova et al. (2018)). Thus we selected MSCWJ-1 long cultivation as model for replicative senescence and examined two structural proteins (myosin-9 and  $\alpha$ -actinin-4) and one regulator responsible for actin cytoskeleton organization and cell motility – small GTPase RhoA (Wang et al. (2003), Elliott et al. (2015)).

Since mammalian nonmuscle myosin II is a key protein in regulation cell motility (Shutova et al. (2017), Shutova and Svitkina (2018)), we investigated its distribution at various passages. We can interpret the spotted pattern ob-

served at passages 15–20 in the case of myosin-9 and  $\alpha$ -actinin-4, as a partial disassembly of the cytoskeletal structures where we see the accumulation of actin-binding proteins in the form of individual particles, or multimolecular protein complexes. Such multimolecular protein complexes, containing myosin-9 and HMW tropomyosin isoforms, was described early (Grenklo et al. (2008), Bobkov and Kropacheva (2017)). We suppose, that the appearance of myosin-9 as additional high molecular band in western blot of fractions 3–4 after gel filtration (approximately 1000 kDa), which we observe at passage 15, is due to the fact that the protein is in the assembly-incompetent form, either as a result of conformational self-inhibition (Vicente-Manzanares et al. (2009)), or as a result of sumoylation (Hofmann et al. (2009), Alonso et al. (2015), Salah et al. (2016)). Both pathways could lead to an observed change in electrophoretic mobility, further research in this direction is needed to shed light on this ambiguity. Assembly-incompetence of myosin-9 at passage 15 is confirmed by immunofluorescence data: myosin-9 appears in aggregates (Fig. 4B), myosin-9/F-actin colocalization level decreases (Fig. 1B).

$\alpha$ -actinin-4 is interesting in that, in addition to well-characterized structural functions, it plays a role in cellular signaling. It was shown that  $\alpha$ -actinins act as negative regulators of myosin stack formation Hu et al. (2019). On the other hand,  $\alpha$ -Actinin-4 was found in nuclei in association with NF- $\kappa$ B transcription factor (Bolshakova et al. (2007), Babakov et al. (2008), Khotin et al. (2009), Lomert et al. (2018)). As critical regulator of cell motility,  $\alpha$ -actinin-4 was shown to induce the epithelial-to-mesenchymal transition and tumorigenesis (Barbolina et al. (2008), Hsu and Kao (2013), An et al. (2016)). Our results demonstrate a decrease in the content of  $\alpha$ -actinin-4 in the nucleus at passage 36, which may indicate a decrease in the signaling function of this protein as a result of cellular senescence. We assume that the detected changes in the myosin-9/F-actin and  $\alpha$ -actinin-4/F-actin colocalization reflect the phenomenon of partial disassembly of the cytoskeleton at passage 15, followed by reassembly at passage 28, which is may be characteristic for switching types of cell movement.

Since the change in the nature of cell movement is due to changes in adhesion and under control of Rho (Huve-neers and Danen (2009)), we decided to reveal RhoA distribution in WJMSC1 cells. The small GTP-binding protein RhoA was initially shown to regulate the assembly of focal adhesions and actin stress fibers in response to growth factors (Ridley and Hall (1992)). It soon became clear that RhoA is one of the central regulators in the organization of the actin cytoskeleton (Burrige and Wennerberg (2004)). In particular, the Rho/ROCK signaling pathway regulates cell motility through the regulation of myosin-9 phosphorylation (Elliott et al. (2015)). Now it's known that RhoA regulates the activity of several transcription regulators and also itself is localized to the nucleus by an as-yet-undiscovered mechanism, therefore the role that RhoA plays in the nucleus is currently being intensively studied (Guilluy et al. (2011), Kim et al. (2018)). Our results demonstrate that the nuclear cytoplasmic RhoA redistribution is involved in the process of cellular aging. At passage 15, the maximum level of RhoA/Hoechst33342 colocalization was detected and the maximum tortuosity of the cell paths was observed at this time point. From 15 to 36 passage, redistribution of RhoA from the nucleus to the cytoplasm occurs, which is accompanied by an increase in the structural integrity of the contractile apparatus and an increase in the straightness of cell tracks. From gel filtration studies we see, that at all investigated passages RhoA elutes in the form of complexes similar in electrophoretic mobility, but passage 28-derived RhoA complex lacks the 100 kDa band. On the other hand, RhoA is detected as a 21 kDa monomer in fraction 3 (approximately 1000 kDa) eluted after passage 15 extract loading. These results indicate structural rearrangements occurring in RhoA cytoplasmic protein complexes, regulating its nuclear cytoplasmic distribution, and require further research in this direction.

Although almost all MSCs in culture are in constant motion, one of the essential signs of replicative senescence is a decrease in cell motility. Until now the cell motility characteristics has not been studied for senescent MSCs in details. Both external and intrinsic factors control directionality of cell movement, therefore it is important to estimate speed characteristics altogether with tortuosity (Tiurin-Kuz'min et al. (2013)). From analysis of cell movement tracks

we conclude that an increase in the contribution of cells with the amoeboid type of movement is maximal at passage 15. Amoeboid cell movements are often characterized by some directional change, which leads to an increase in the tortuosity of the movement tracks (Li et al. (2008)). In general, we can interpret the data on mobility in such a way that the old cells compensate for the decrease in the speed of movement with an increase in straightness, which leads to the same average distance crawled by the cells at 15 and 36 passages. Old cells with reduced proliferative potential and speed characteristics seem to follow the motto “No time for random walks - just keep moving forward”.

The actin cytoskeleton of non-muscle cells is a highly dynamic system and is constantly in the state of assembly/disassembly, therefore it is important to pay attention not only to the assembled structures reshown by various forms of F-actin stabilized by actin-binding proteins, but also to study the set of proteins corresponding to the disassembled cytoskeleton. The distribution of proteins in fractions after gel filtration allows us to evaluate the structural features of the organization of a set of proteins that are not included in the cytoskeleton structures. We investigated the distribution of  $\beta$ -actin in the fractions obtained by gel filtration of MSCWJ-1 cytosole extracts, because this isoactin is the main one in non-muscle cells (Khaitlina (2001)). In young cells at passage 9,  $\beta$ -actin is detected as a single peak in fraction 11, which corresponds to the size of the monomeric protein. As a result of cellular senescence,  $\beta$ -actin forms additional peaks in fractions of 6-7 (approximately 500 kDa) at passages 15 and 36, which suggests that  $\beta$ -actin forms complexes with other proteins. It can be assumed that  $\beta$ -actin forms stable cytoplasmic complexes with cofilin or other sequestering monomeric actin proteins. Additional research including immunoprecipitation and mass-spectrometry are needed to clarify this assumption.

Thus, the totality of our results allows us to divide the process of replicative aging into two stages, which are followed on the background of a steady decrease in the speed of movement of cells. The first stage lasts from thawing to passage 15 and characterized by a decrease in myosin-9/F-actin and  $\alpha$ -actinin-4/F-actin colocalization, by nuclear RhoA level increase, and by path tortuosity increase. The second stage covers passages 15 – 36 and is characterized by an increase in the structural integrity of the actin cytoskeleton, nuclear exit of RhoA and  $\alpha$ -actinin-4 and decrease in path tortuosity.

## 4 | EXPERIMENTAL PROCEDURES

### 4.1 | Cell cultures: MSCWJ-1

A line of human mesenchymal stem cells obtained from Varton's jelly of the human umbilical cord (MSCWJ-1) were obtained from "Collection of vertebrate cell cultures" of the Institute of Cytology of the Russian Academy of Sciences (INC RAS, Russia, St. Petersburg). Main characteristics confirming the status of MSCs for MSCWJ-1, according to the requirements of the International Society for Cellular Therapy, were published previously (Krylova et al. (2017), Koltsova et al. (2018), Dominici et al. (2006); Sensebe et al. (2010)). MSCWJ-1 cells were cultured in growth medium containing 90% DMEM/F12 medium (Biolot, Russia, St. Petersburg) and 10% FBS (Hyclone, USA, Texas). Cells were cultured in 5%  $CO_2$ , 37°C and 90% humidity conditions. Microbiological analysis confirmed the absence of bacterial, fungal and mycoplasmal contamination in the resulting line.

### 4.2 | Replicative cell senescence

The efficacy of the  $\beta$ -galactosidase enzyme was evaluated by the  $\beta$ -galactosidase enzyme activity. MSCWJ-1 cells were grown in 3 cm dishes until subconfluent formation and fixed at passages 9, 8, 15, 28. Then the medium was removed and the cells were stained using a reagent kit (Senescence  $\beta$ -galactosidase staining kit; Cell Signaling, USA,

Massachusetts). In cells entering the phase of replicative senescence, the cytoplasm has a bright blue color. The analysis was performed using an inverted microscope equipped with 60x objective (Nikon, Japan, Tokyo). The percentage of stained cells in percent was determined by counting at least 1000 cells in different fields of view at each passage. The results were processed statistically as described further.

### 4.3 | Immunofluorescence

Coverslips with adherent cells were fixed in a 3% solution of paraformaldehyde for 10 min at room temperature and permeabilized in a solution of 0.1% TritonX-100 for 10 min at room temperature, then the coverslips with cells was poured with 1% BSA solution for 20 min. Rabbit polyclonal antibodies produced against the N-terminal peptide of the heavy chain of nonmuscle myosin IIA, rabbit polyclonal antibodies produced against the  $\alpha$ -actinin-4 and mouse monoclonal antibodies produced against the RhoA were used as the first antibodies (Sigma-Aldrich, USA, Missouri). Goat antibodies to the Alexa fluor 488 rabbit antigens (Invitrogen, USA, California) were used as second antibodies. To visualize the actin cytoskeleton, cells were stained with rhodamine phalloidin for 20 min at room temperature. Nuclei were stained with Hoechst33342 at final concentration 1.5  $\mu$ g/mL, then preparations were made with ProLong Gold antifade reagent (Thermo Fisher, USA, Massachusetts). were examined using an inverted Leica TCS SP8 laser scanning confocal microscope equipped with a resonance scanner and with a x63 oil immersion lense (Leica, Germany, Wetzlar). To the simultaneous detection of fluorescence of Alexa 488 and rhodamine phalloidin we used an argon laser with 488 nm wavelength and HeNe laser with 543 nm wavelength. Fluorescence detection was carried out using two photomultiplier tubes in the spectral range 493–540 nm for Alexa 488 and 552–792 nm for rhodamine-phalloidin.

### 4.4 | Colocalization analysis

Colocalization coefficients were calculated using ImageJ version 1.52i using the Coloc 2 plugin (Rueden et al. (2017)). Raw 1024 x 1024 px images was in 72 dpi resolution. For colocalization analysis images were opened in ImageJ, RGB channels were converted to 32 bit grayscale. Data collected in two channels from manually adjusted ROIs in confocal images with MSCWJ-1 cells stained with polyclonal anti-myosin-9 antibodies and rhodamine phalloidin. Cells were fixed at passages: 7, 9, 12, 15, 18, 21, 25, 27, 28, 35, 36. Cells were selected manually on merged image and ROI passed to Coloc2 plugin. The bTau, Rval, Rs, tM1, tM2 colocalization coefficients were calculated and passed as CSV files to R environment (Adler et al. (2008); Bergholm et al. (2010)).

We conducted PCA in order to identify the colocalization coefficient most suitable for our purposes. The results shown in Supplementary. Shortly, bTau and Rs coefficients shows very high correlation, tM1 and Rval coefficient shows moderate correlation. Kruskal-Wallis rank sum test results suggest that bTau reflects changes in colocalization so well. The PCA and factor analysis allowed us to conclude that bTau is the most suitable coefficient and in the future we use it for the analysis of cytoskeletal rearrangements. In further analysis, the values of the bTau shown were interpreted in accordance with the Cheddock scale (see table 1 in Supplementary).

### 4.5 | Quantitative image cytometry and cell movement analysis

Comparative analysis of cell movement characteristics relative to replicative senescence was performed using time-lapse imaging. For recording the movement of individual cells we used high-content Quantitative Image Cytometer CQ1 (Yokogawa, Japan, Tokyo) with spinning disk confocal technology (Sakashita et al. (2015)). Cells were plated on 6-well dishes and stained with Hoechst 33342 (Invitrogen, USA, California). Images were acquired during 24 h session



with 405-nm laser and bright field illumination using 40x 0.95-NA dry objective lens. All images had a 2560 x 2160 pixel resolution, with a pixel size equivalent to 1.3158  $\mu\text{m}$  in x and y. A set of x-y coordinates were obtained from images in ImageJ software with Manual tracking plugin. Each cell was manually marked in the middle of the nucleus in each time point. Only cells satisfying the following conditions were noted: the cell must be in the field of view in all frames, the cell does not divide. Dividing cells were not counted. Trajectories were obtained from a set of x-y coordinates. The resulting tracks were combined into a data frame and analyzed in the R environment using trajr package (McLean and Skowron Volponi (2018)), which is a suitable toolkit for the numerical characterisation and analysis of the trajectories of moving cells. Trajectory coordinates were read from a CSV data file, and then passed in to the trajectory analysis functions. Trajectories were resampled to 15 min fixed step length by rediscretization function using the algorithm described by Bovet & Benhamou (Bovet and Benhamou (1988)). As a result of the analysis of the trajectories, we obtained the following parameters: total length of the trajectory, straight-line distance from the start to the end of the trajectory, mean and maximum speeds, straightness and sinuosity indexes. To measure the straightness, or conversely, tortuosity, of trajectories, we used two indexes. The simplest is straightness index and computed as  $D/L$ , where  $D$  is the distance from the start to the end of the trajectory, and  $L$  is the length of the trajectory. This straightness index is a number ranging from 0 to 1, where 1 indicates a straight line. The straightness index is considered to be a reliable measure of the efficiency of a directed walk, but inapplicable to random trajectories. The sinuosity index defined by Benhamou (Benhamou (2004)) may be an appropriate measure of the tortuosity of a random search path. Sinuosity is a function of the mean cosine of turning angles, and is a corrected form of the original sinuosity index defined by Bovet and Benhamou (Bovet and Benhamou (1988)).

#### 4.6 | FPLC gel filtration

For gel-chromatographic separation of cell extracts, an FPLC system (Pharmacia, Sweden, Stockholm) equipped with Superose 6 column (GE, USA, Massachusetts) was used. Signal detection was performed using chromatograph Millichrom A02 detection unit (Econova Ltd., Russia, Novosibirsk). Elution was performed with elution buffer (150 mM NaCl, 50 mM Tris, pH 7.5, 0.02%  $NaNO_3$ ). The column was calibrated with the set of proteins shown in Table 2 in Supplementary.

Cells were grown on 10 cm dishes (12 dishes for each passage) and lysed at passages 9, 15, 28. Cytosolic cell extracts were prepared as described in our previous work, briefly, formaldehyde cross-links were preliminarily created in the cells to protect the protein complexes from degradation, then the cells were lysed with a buffer preserving the F/G actin ratio (Bobkov and Kropacheva (2017)) with addition of protease inhibitors cocktail (Sigma-Aldrich, USA, Missouri). In order to prevent the destruction of multimolecular protein complexes, in the first stage the medium in the plates was replaced with medium containing 10  $\mu\text{M}$  formaldehyde, incubated for 10 minutes at 37° C, then a solution of glycine at a concentration of 1.875 g per 200 ml was added to each cup PBS, incubated for 5-7 min at 37° C. Subsequently, we washed the cups after glycine with a solution of PBS and poured 20  $\mu\text{l}$  of protease inhibitor and 1 ml of lysis buffer was left for 1 min on ice. Next, the method of sequential selection of cell extract was collected in the ependorf 1 ml of the sample. The final stage of lizing was centrifugation for 10 min at 24000 RCF and freezing of the samples at -80 ° C. The protein extract was filtered and applied to the column in a volume of 500  $\mu\text{l}$ . Fractions were collected on ice 1 ml each 2 min starting from time point determined by calibration set separation. For protein sedimentation, 100  $\mu\text{l}$  of 0.15% DOX was added to the collected fractions and mixed vigorously, incubated for 10 min at -20° C, then 100  $\mu\text{l}$  of 50% TCA was added, mixed, incubated for 15 minutes at -20° C. Protein precipitation was carried out by 30 min centrifugation at 24000 RCF at +4° C. The supernatant was removed, and cold 100% acetone was added to the precipitate, mixed vigorously and incubated for 12 hours at -20° C. A repeated washing with acetone

was done, and then the protein was precipitated by centrifugation for 15 min at 24000 RCF at +4° C, the supernatant was collected, the precipitate was dried, and 2-fold sample buffer was added to the precipitate (125 mM Tris-HCl, pH 6.8, 4% SDS, 10% glycerol, 0.006% bromo-phenol blue, 1.8%  $\beta$ -mercaptoethanol). Samples were heated for 10 minutes at 98° C, probes were stored at -20° C before electrophoretic separation.

#### 4.7 | Electrophoresis and western blot

Proteins were separated by electrophoresis in a 12.5% polyacrylamide gel under denaturing conditions in the presence of SDS (Laemmli (1970)). After electrophoresis, the gel was stained with Coomassie brilliant blue or carried out by Western blotting (Towbin et al. (1979)). Protein transfer from the gel to the Immobilon-P membrane (Millipore, USA, Massachusetts) was carried out in Tris-glycine buffer pH 8.3, containing 10% ethanol and 0.1% SDS. Western blotting was performed according to the ECL protocol (Amersham, UK, Little Chalfont). After transferring, the membrane was washed for 20 minutes with PBS containing 0.1% tween-20 and blocked non-specific binding sites with 5% non-fat dry milk diluted in PBS for 1 hour. The membrane was incubated with the first antibodies for 1 hour at room temperature three times. washed in PBS, stained with second antibodies for 1 h at room temperature. Rabbit polyclonal antibodies produced against the N-terminal peptide of myosin-9, mouse monoclonal anti- $\beta$ -actin antibodies (clone AC-15) were used as the first antibodies. Rabbit antibodies to mouse antigens and goat antibodies to rabbit antigens conjugated with HRP were used as second antibodies (Sigma-Aldrich, USA, Missouri). To enhance the signal in western blotting, SuperSignal substrate (Thermo Scientific, USA, Massachusetts) was used. Chemiluminescent radiation was recorded using a ChemiDoc Touch system (Bio-Rad, USA, California).

#### 4.8 | Description of statistical analysis methods

The study materials were subjected to statistical processing using the methods of parametric and non-parametric analysis. The accumulation, correction, systematization of the initial information were carried out in Office Excel 2016 spreadsheets (Microsoft, USA, Washington). Statistical analysis was done using the free software computing environment R v. 3.5.3 (Team et al. (2014)).

The data obtained from  $\beta$ -Galactosidase activity assay were computed following the Wilson method to obtain 95 % confidence intervals for binomial proportions (Wilson (1927)).

The data obtained from measurements of the colocalization coefficient were combined into variational series, in which the arithmetic mean values and SDs were calculated. PCA, generalized linear model and maximum-likelihood factor analysis were performed if R environment (Husson et al. (2010), Dobson and Barnett (2008), Lawley and Maxwell (1971)).

In the course of all-pairs comparisons of colocalization data post hoc multiple testing corrections were used to adjust the P-values: Mann-Whitney rank test, Bonferroni method, Scheffe's, and Dunn's tests (Fig. S1). The results were visualized using the free Python computing software environment and the scikit-posthocs package (Terpilowski (2019)).

The data obtained from trajectory analysis were cleaned from outliers: those observations that deviate from the 1st or 3rd quartile by more than one and a half interquartile range were deleted. Quantitative indicators were evaluated for compliance with the normal distribution, for this purpose, the Shapiro – Wilk criterion was used with  $n > 170$  (Shapiro and Wilk (1965); Shapiro and Francia (1972)) as well as indicators of asymmetry and kurtosis (see Supplementary for details). When comparing several samples of quantitative data with a distribution other than normal, Kruskal-Wallis criterion was used, which is a non-parametric alternative to single-factor analysis of variance (Kruskal

and Wallis (1952)). In the event that the calculated value of the Kruskal-Wallis criterion exceeded the critical one, the differences in the indicators were considered statistically significant (Wilcoxon (1992)).

Data and scripts used to generate the analyses are available via data repository on Github : <https://github.com/Dan609/myo>.

## Author contributions

Author1 and Author6 designed the research, analyzed the data, wrote the article. Author2 carried out immunofluorescence and western blotting. Author3 maintained cell line and made the  $\beta$ -galactosidase test. Author4 carried out intravital confocal cytometry. Author5 made the chromatographic separation.

## Acknowledgements

We are thankful to Dr. G. Stein and M. Vorobyov for their expert assistance in confocal microscopy. We are thankful to S. Boykov for assistance in computational trajectory analysis. We acknowledge I. Kropacheva and Dr. A. Koltsova for technical help and general support. We are thankful to Dr. XY for providing financial funding. We appreciate Dr. Edvard's help in manuscript language proof reading.

## Conflict of interest

The authors declare no conflict of interest.

## References

- Adler, J., Pagakis, S. and Parmryd, I. (2008) Replicate-based noise corrected correlation for accurate measurements of colocalization. *Journal of microscopy*, **230**, 121–133.
- Alessio, N., Pipino, C., Mandatori, D., Di Tomo, P., Ferone, A., Marchiso, M., Melone, M. A., Peluso, G., Pandolfi, A. and Galderisi, U. (2018) Mesenchymal stromal cells from amniotic fluid are less prone to senescence compared to those obtained from bone marrow: an in vitro study. *Journal of cellular physiology*, **233**, 8996–9006.
- Alonso, A., Greenlee, M., Matts, J., Kline, J., Davis, K. J. and Miller, R. K. (2015) Emerging roles of sumoylation in the regulation of actin, microtubules, intermediate filaments, and septins. *Cytoskeleton*, **72**, 305–339.
- An, H., Yoo, S. and Ko, J. (2016)  $\alpha$ -actinin-4 induces the epithelial-to-mesenchymal transition and tumorigenesis via regulation of snail expression and  $\beta$ -catenin stabilization in cervical cancer. *Oncogene*, **35**, 5893.
- Ando, Y., Matsubara, K., Ishikawa, J., Fujio, M., Shohara, R., Hibi, H., Ueda, M. and Yamamoto, A. (2014) Stem cell-conditioned medium accelerates distraction osteogenesis through multiple regenerative mechanisms. *Bone*, **61**, 82–90.
- Babakov, V. N., Petukhova, O. A., Turoverova, L. V., Kropacheva, I. V., Tentler, D. G., Bolshakova, A. V., Podolskaya, E. P., Magnusson, K.-E. and Pinaev, G. P. (2008) RelA/nf- $\kappa$ b transcription factor associates with  $\alpha$ -actinin-4. *Experimental cell research*, **314**, 1030–1038.

- Barbolina, M. V., Adley, B. P., Kelly, D. L., Fought, A. J., Scholtens, D. M., Shea, L. D. and Stack, M. S. (2008) Motility-related actinin alpha-4 is associated with advanced and metastatic ovarian carcinoma. *Laboratory investigation*, **88**, 602.
- Benhamou, S. (2004) How to reliably estimate the tortuosity of an animal's path: straightness, sinuosity, or fractal dimension? *Journal of theoretical biology*, **229**, 209–220.
- Bergholm, F., Adler, J. and Parmryd, I. (2010) Analysis of bias in the apparent correlation coefficient between image pairs corrupted by severe noise. *Journal of Mathematical Imaging and Vision*, **37**, 204–219.
- Bertolo, A., Gemperli, A., Gruber, M., Gantenbein, B., Baur, M., Pötzel, T. and Stoyanov, J. (2015) In vitro cell motility as a potential mesenchymal stem cell marker for multipotency. *Stem cells translational medicine*, **4**, 84–90.
- Bobkov, D. and Kropacheva, I. (2017) The effect of lysophosphatidic acid on the composition of cytoplasmic protein complexes that contain myosin-9 and tropomyosin. *Cell and Tissue Biology*, **11**, 197–204.
- Bolshakova, A., Petukhova, O., Turoverova, L., Tentler, D., Babakov, V., Magnusson, K.-E. and Pinaev, G. (2007) Extracellular matrix proteins induce re-distribution of  $\alpha$ -actinin-1 and  $\alpha$ -actinin-4 in a431 cells. *Cell biology international*, **31**, 360–365.
- Bovet, P. and Benhamou, S. (1988) Spatial analysis of animals' movements using a correlated random walk model. *Journal of theoretical biology*, **131**, 419–433.
- Burridge, K. and Wennerberg, K. (2004) Rho and rac take center stage. *Cell*, **116**, 167–179.
- Carvalho, M. M., Teixeira, G. F., Rui, R. L., Sousa, N. and J Salgado, A. (2011) Mesenchymal stem cells in the umbilical cord: phenotypic characterization, secretome and applications in central nervous system regenerative medicine. *Current stem cell research & therapy*, **6**, 221–228.
- Danieli, P., Malpasso, G., Ciuffreda, M. C. and Gnechi, M. (2016) Testing the paracrine properties of human mesenchymal stem cells using conditioned medium. In *Mesenchymal Stem Cells*, 445–456. Springer.
- Danisovic, L., Oravcova, L., Krajciova, L., Varchulova Novakova, Z., Bohac, M., Varga, I. and Vojtassak, J. (2017) Effect of long-term culture on the biological and morphological characteristics of human adipose tissue-derived stem cells. *J Physiol Pharmacol*, **68**, 149–158.
- Dobson, A. J. and Barnett, A. G. (2008) *An introduction to generalized linear models*. Chapman and Hall/CRC.
- Dominici, M., Le Blanc, K., Mueller, I., Slaper-Cortenbach, I., Marini, F., Krause, D., Deans, R., Keating, A., Prockop, D. and Horwitz, E. (2006) Minimal criteria for defining multipotent mesenchymal stromal cells. the international society for cellular therapy position statement. *Cytotherapy*, **8**, 315–317.
- Elliott, H., Fischer, R. S., Myers, K. A., Desai, R. A., Gao, L., Chen, C. S., Adelstein, R. S., Waterman, C. M. and Danuser, G. (2015) Myosin ii controls cellular branching morphogenesis and migration in three dimensions by minimizing cell-surface curvature. *Nature cell biology*, **17**, 137.
- Estrada, J. C., Torres, Y., Benguria, A., Dopazo, A., Roche, E., Carrera-Quintanar, L., Pérez, R., Enriquez, J. A., Torres, R., Ramirez, J. C. et al. (2013) Human mesenchymal stem cell-replicative senescence and oxidative stress are closely linked to aneuploidy. *Cell death & disease*, **4**, e691.

- Geißler, S., Textor, M., Kühnisch, J., Könning, D., Klein, O., Ode, A., Pfitzner, T., Adjaye, J., Kasper, G. and Duda, G. N. (2012) Functional comparison of chronological and in vitro aging: differential role of the cytoskeleton and mitochondria in mesenchymal stromal cells. *PLoS one*, **7**, e52700.
- Grenklo, S., Hillberg, L., Rathje, L.-S. Z., Pinaev, G., Schutt, C. E. and Lindberg, U. (2008) Tropomyosin assembly intermediates in the control of microfilament system turnover. *European journal of cell biology*, **87**, 905–920.
- Gruenloh, W., Kambal, A., Sondergaard, C., McGee, J., Nacey, C., Kalomoiris, S., Pepper, K., Olson, S., Fierro, F. and Nolte, J. A. (2011) Characterization and in vivo testing of mesenchymal stem cells derived from human embryonic stem cells. *Tissue engineering Part A*, **17**, 1517–1525.
- Guiducci, S., Manetti, M., Romano, E., Mazzanti, B., Ceccarelli, C., Dal Pozzo, S., Milia, A. F., Bellando-Randone, S., Fiori, G., Conforti, M. L. et al. (2011) Bone marrow-derived mesenchymal stem cells from early diffuse systemic sclerosis exhibit a paracrine machinery and stimulate angiogenesis in vitro. *Annals of the rheumatic diseases*, **70**.
- Guilluy, C., Dubash, A. D. and García-Mata, R. (2011) Analysis of rhoA and rho GEF activity in whole cells and the cell nucleus. *Nature protocols*, **6**, 2050.
- Hayflick, L. and Moorhead, P. S. (1961) The serial cultivation of human diploid cell strains. *Experimental cell research*, **25**, 585–621.
- Hendijani, F., Javanmard, S. H., Rafiee, L. and Sadeghi-Aliabadi, H. (2015a) Effect of human wharton's jelly mesenchymal stem cell secretome on proliferation, apoptosis and drug resistance of lung cancer cells. *Research in pharmaceutical sciences*, **10**, 134.
- Hendijani, F., Javanmard, S. H. and Sadeghi-Aliabadi, H. (2015b) Human wharton's jelly mesenchymal stem cell secretome display antiproliferative effect on leukemia cell line and produce additive cytotoxic effect in combination with doxorubicin. *Tissue and Cell*, **47**, 229–234.
- Hofmann, W. A., Arduini, A., Nicol, S. M., Camacho, C. J., Lessard, J. L., Fuller-Pace, F. V. and de Lanerolle, P. (2009) Sumoylation of nuclear actin. *The Journal of cell biology*, **186**, 193–200.
- Hsu, K.-S. and Kao, H.-Y. (2013) Alpha-actinin 4 and tumorigenesis of breast cancer. In *Vitamins & Hormones*, vol. 93, 323–351. Elsevier.
- Hu, S., Grobe, H., Guo, Z., Wang, Y.-H., Doss, B. L., Pan, M., Ladoux, B., Bershadsky, A. D. and Zaidel-Bar, R. (2019) Reciprocal regulation of actomyosin organization and contractility in non-muscle cells by tropomyosins and alpha-actinins. *Molecular Biology of the Cell*, mbc-E19.
- Huang, Y.-C., Leung, V. Y., Lu, W. W. and Luk, K. D. (2013) The effects of microenvironment in mesenchymal stem cell-based regeneration of intervertebral disc. *The Spine Journal*, **13**, 352–362.
- Husson, F., Lê, S. and Pages, J. (2010) Exploratory multivariate analysis by example using R, volume 20105550 of Chapman & Hall/CRC computer science & data analysis. CRC Press, **30**, 101–102.
- Huveneers, S. and Danen, E. H. (2009) Adhesion signaling—crosstalk between integrins, Src and Rho. *Journal of cell science*, **122**, 1059–1069.

- Julianto, I. and Rindastuti, Y. (2016) Topical delivery of mesenchymal stem cells" secretomes" in wound repair. *Acta Medica Indonesiana*, **48**, 217–220.
- Khaitlina, S. Y. (2001) Functional specificity of actin isoforms. *International Review of Cytology*, **202**, 35–98.
- Khotin, M., Turoverova, L., Podolskaya, E., Krasnov, I., Solovyeva, A., Aksenova, V. Y., Magnusson, K.-E., Pinaev, G. and Tentler, D. (2009) Analysis of nuclear protein complexes comprising  $\alpha$ -actinin-4 by 2d-electrophoresis and mass spectrometry. *Cell and Tissue Biology*, **3**, 431.
- Kim, J.-G., Islam, R., Cho, J. Y., Jeong, H., Cap, K.-C., Park, Y., Hossain, A. J. and Park, J.-B. (2018) Regulation of rhoa gtpase and various transcription factors in the rhoa pathway. *Journal of cellular physiology*, **233**, 6381–6392.
- Koltsova, A., Krylova, T., Musorina, A., Zenin, V., Turilova, V., Yakovleva, T. and Poljanskaya, G. (2018) The dynamics of cell properties during long-term cultivation of two lines of mesenchymal stem cells derived from wharton's jelly of human umbilical cord. *Cell and Tissue Biology*, **12**, 7–19.
- Kruskal, W. H. and Wallis, W. A. (1952) Use of ranks in one-criterion variance analysis. *Journal of the American statistical Association*, **47**, 583–621.
- Krylova, T., Koltsova, A., Musorina, A., Zenin, V., Turilova, V., Yakovleva, T. and Poljanskaya, G. (2017) Derivation and characteristic of two lines of human mesenchymal stem cells, generated from the wharton's jelly of the human umbilical cord. *Tsitologiya*, **59**, 315–327.
- Krylova, T., Musorina, A., Koltsova, A., Zenin, V., Turilova, V., Yakovleva, T. and Poljanskaya, G. (2018) Isolation and comparative characteristics of mesenchymal stem-cell lines derived from foreskin of two donors of similar age. *Cell and Tissue Biology*, **12**, 271–280.
- Kuilman, T., Michaloglou, C., Mooi, W. J. and Peeper, D. S. (2010) The essence of senescence. *Genes & development*, **24**, 2463–2479.
- Laemmli, U. K. (1970) Cleavage of structural proteins during the assembly of the head of bacteriophage t4. *nature*, **227**, 680.
- Larsen, M., Tremblay, M. L. and Yamada, K. M. (2003) Phosphatases in cell–matrix adhesion and migration. *Nature reviews Molecular cell biology*, **4**, 700.
- Lawley, D. N. and Maxwell, A. E. (1971) Factor analysis as statistical method. *Tech. rep.*
- Le Clainche, C. and Carlier, M.-F. (2008) Regulation of actin assembly associated with protrusion and adhesion in cell migration. *Physiological reviews*, **88**, 489–513.
- Li, L., Nørrelykke, S. F. and Cox, E. C. (2008) Persistent cell motion in the absence of external signals: a search strategy for eukaryotic cells. *PLoS one*, **3**, e2093.
- Lomert, E., Turoverova, L., Kriger, D., Aksenov, N. D., Nikotina, A. D., Petukhov, A., Mittenberg, A. G., Panyushev, N. V., Khotin, M., Volkov, K. et al. (2018) Co-expression of rela/p65 and actn4 induces apoptosis in non-small lung carcinoma cells. *Cell Cycle*, **17**, 616–626.

- Luo, J., Zhao, X., Tan, Z., Su, Z., Meng, F. and Zhang, M. (2013) Mesenchymal-like progenitors derived from human embryonic stem cells promote recovery from acute kidney injury via paracrine actions. *Cytotherapy*, **15**, 649–662.
- McLean, D. J. and Skowron Volponi, M. A. (2018) trajr: An r package for characterisation of animal trajectories. *Ethology*, **124**, 440–448.
- Moujaber, O., Fishbein, F., Omran, N., Liang, Y., Colmegna, I., Presley, J. F. and Stochaj, U. (2019) Cellular senescence is associated with reorganization of the microtubule cytoskeleton. *Cellular and Molecular Life Sciences*, 1–15.
- Niedernhofer, L. J., Gurkar, A. U., Wang, Y., Vijg, J., Hoeijmakers, J. H. and Robbins, P. D. (2018) Nuclear genomic instability and aging. *Annual review of biochemistry*, **87**, 295–322.
- Omelchenko, T., Vasiliev, J., Gelfand, I., Feder, H. and Bonder, E. (2002) Mechanisms of polarization of the shape of fibroblasts and epitheliocytes: Separation of the roles of microtubules and rho-dependent actin-myosin contractility. *Proceedings of the National Academy of Sciences*, **99**, 10452–10457.
- Özcan, S., Alessio, N., Acar, M. B., Mert, E., Omerli, F., Peluso, G. and Galderisi, U. (2016) Unbiased analysis of senescence associated secretory phenotype (sasp) to identify common components following different genotoxic stresses. *Aging (Albany NY)*, **8**, 1316.
- Phinney, D. G. and Prockop, D. J. (2007) Concise review: mesenchymal stem/multipotent stromal cells: the state of transdifferentiation and modes of tissue repair—current views. *Stem cells*, **25**, 2896–2902.
- Redaelli, S., Bentivegna, A., Foudah, D., Miloso, M., Redondo, J., Riva, G., Baronchelli, S., Dalprà, L. and Tredici, G. (2012) From cytogenomic to epigenomic profiles: monitoring the biologic behavior of in vitro cultured human bone marrow mesenchymal stem cells. *Stem cell research & therapy*, **3**, 47.
- Ridley, A. J. and Hall, A. (1992) The small gtp-binding protein rho regulates the assembly of focal adhesions and actin stress fibers in response to growth factors. *Cell*, **70**, 389–399.
- Rueden, C. T., Schindelin, J., Hiner, M. C., DeZonia, B. E., Walter, A. E., Arena, E. T. and Eliceiri, K. W. (2017) ImageJ2: Imagej for the next generation of scientific image data. *BMC bioinformatics*, **18**, 529.
- Sakashita, H., Ohashi, K., Ozawa, K. and Tsubouchi, Y. (2015) The cq1 confocal quantitative image cytometer and its application to biological measurement. *Tech. rep.*, Yokogawa Technical Report English Edition.
- Salah, H., Li, M., Cacciani, N., Gastaldello, S., Ogilvie, H., Akkad, H., Namuduri, A. V., Morbidoni, V., Artemenko, K. A., Balogh, G. et al. (2016) The chaperone co-inducer bgp-15 alleviates ventilation-induced diaphragm dysfunction. *Science translational medicine*, **8**, 350ra103–350ra103.
- Savickienė, J., Baronaitė, S., Zentelytė, A., Treigytė, G. and Navakauskienė, R. (2016) Senescence-associated molecular and epigenetic alterations in mesenchymal stem cell cultures from amniotic fluid of normal and fetus-affected pregnancy. *Stem cells international*, **2016**.
- Sensebe, L., Krampera, M., Schrezenmeier, H., Bourin, P. and Giordano, R. (2010) Mesenchymal stem cells for clinical application. *Vox sanguinis*, **98**, 93–107.
- Shapiro, S. S. and Francia, R. (1972) An approximate analysis of variance test for normality. *Journal of the American Statistical Association*, **67**, 215–216.

- Shapiro, S. S. and Wilk, M. B. (1965) An analysis of variance test for normality (complete samples). *Biometrika*, **52**, 591–611.
- Shutova, M. S., Asokan, S. B., Talwar, S., Assoian, R. K., Bear, J. E. and Svitkina, T. M. (2017) Self-sorting of nonmuscle myosins iia and iib polarizes the cytoskeleton and modulates cell motility. *J Cell Biol*, **216**, 2877–2889.
- Shutova, M. S. and Svitkina, T. M. (2018) Mammalian nonmuscle myosin ii comes in three flavors. *Biochemical and biophysical research communications*, **506**, 394–402.
- Team, R. C. et al. (2014) R: A language and environment for statistical computing. *R*.
- Teixeira, F. G., Carvalho, M. M., Panchalingam, K. M., Rodrigues, A. J., Mendes-Pinheiro, B., Anjo, S., Manadas, B., Behie, L. A., Sousa, N. and Salgado, A. J. (2017) Impact of the secretome of human mesenchymal stem cells on brain structure and animal behavior in a rat model of parkinson's disease. *Stem cells translational medicine*, **6**, 634–646.
- Terpilowski, M. (2019) scikit-posthocs: Pairwise multiple comparison tests in python. *The Journal of Open Source Software*, **4**, 1169.
- Tiurin-Kuz'min, P., Vorotnikov, A. and Tkachuk, V. (2013) Molecular mechanisms of gradient sensing in mesenchymal cells. *Rossiiskii fiziologicheskii zhurnal imeni IM Sechenova*, **99**, 294–312.
- Towbin, H., Staehelin, T. and Gordon, J. (1979) Electrophoretic transfer of proteins from polyacrylamide gels to nitrocellulose sheets: procedure and some applications. *Proceedings of the National Academy of Sciences*, **76**, 4350–4354.
- Truong, N. C., Bui, K. H.-T. and Van Pham, P. (2018) Characterization of senescence of human adipose-derived stem cells after long-term expansion.
- Turinetto, V., Vitale, E. and Giachino, C. (2016) Senescence in human mesenchymal stem cells: functional changes and implications in stem cell-based therapy. *International journal of molecular sciences*, **17**, 1164.
- Vasiliev, J. (1991) Polarization of pseudopodial activities: cytoskeletal mechanisms. *Journal of Cell Science*, **98**, 1–4.
- Vicente-Manzanares, M., Ma, X., Adelstein, R. S. and Horwitz, A. R. (2009) Non-muscle myosin ii takes centre stage in cell adhesion and migration. *Nature reviews Molecular cell biology*, **10**, 778.
- Vulcano, F., Milazzo, L., Ciccarelli, C., Eramo, A., Sette, G., Mauro, A., Macioce, G., Martinelli, A., La Torre, R., Casalbore, P. et al. (2016) Wharton's jelly mesenchymal stromal cells have contrasting effects on proliferation and phenotype of cancer stem cells from different subtypes of lung cancer. *Experimental cell research*, **345**, 190–198.
- Wagner, W., Horn, P., Castoldi, M., Diehlmann, A., Bork, S., Saffrich, R., Benes, V., Blake, J., Pfister, S., Eckstein, V. et al. (2008) Replicative senescence of mesenchymal stem cells: a continuous and organized process. *PloS one*, **3**, e2213.
- Wang, D. and Jang, D.-J. (2009) Protein kinase ck2 regulates cytoskeletal reorganization during ionizing radiation-induced senescence of human mesenchymal stem cells. *Cancer research*, **69**, 8200–8207.
- Wang, H.-R., Zhang, Y., Ozdamar, B., Ogunjimi, A. A., Alexandrova, E., Thomsen, G. H. and Wrana, J. L. (2003) Regulation of cell polarity and protrusion formation by targeting rhoa for degradation. *Science*, **302**, 1775–1779.



- Wilcoxon, F. (1992) Individual comparisons by ranking methods. In *Breakthroughs in statistics*, 196–202. Springer.
- Wilson, E. B. (1927) Probable inference, the law of succession, and statistical inference. *Journal of the American Statistical Association*, **22**, 209–212.
- Yu, J., Shi, J., Zhang, Y., Zhang, Y., Huang, Y., Chen, Z. and Yang, J. (2018) The replicative senescent mesenchymal stem/stromal cells defect in dna damage response and anti-oxidative capacity. *International journal of medical sciences*, **15**, 771.
- Zachar, L., Bačenková, D. and Rosocha, J. (2016) Activation, homing, and role of the mesenchymal stem cells in the inflammatory environment. *Journal of inflammation research*, **9**, 231.
- Zhang, T., Wang, P., Liu, Y., Zhou, J., Shi, Z., Cheng, K., Huang, T., Wang, X., Yang, G. L., Yang, B. et al. (2018) Over-expression of foxq1 enhances anti-senescence and migration effects of human umbilical cord mesenchymal stem cells in vitro and in vivo. *Cell and tissue research*, **373**, 379–393.

## Supporting Information

Supplementary with statistical tests results. Video files with cell tracking.

## Figure legends

### | Figure 1

(A) Staining of F-actin (red) and myosin-9 (green) and nuclei (blue on merged images) in MSCWJ-1. Cells were grown on glasses, fixed and permeabilised at passages 9, 15, 36. Polyclonal antibodies against synthetic peptide corresponding to amino acids 1949-1960 of human nonmuscle myosin IIA and Alexa 488 secondary anti-rabbit antibodies were used for myosin-9 staining. Hoechst33342 was used for nuclei staining. Rhodamine phalloidin was used to stain actin cytoskeleton. (B) Myosin-9/F-actin colocalization in MSCWJ-1. Cells were grown on glasses, fixed and permeabilised at passages 7, 9, 12, 15, 18, 21, 25, 27, 28, 35, 36. F-actin and myosin-9 were stained as previously indicated. Ten fields of view were recorded using confocal microscopy, cells were manually selected on merged images and Kendall's colocalization coefficient (bTau) was measured in ImageJ, then data passed to R environment for statistical analysis. Boxplots shown over jitter plots. In jitter plots each point represents one observation. In boxplots horizontal lines indicate 1st quartile, mean 3d quartile, whiskers indicate range. Significant differences identified by the Wilcoxon test are indicated by p-values shown on square brackets. (C) In the course of all-pairs comparisons of colocalization data post hoc multiple Mann-Whitney rank test was used to adjust the P-values. The results were visualized using the free Python computing software environment and the scikit-posthocs package (Terpilowski (2019)) For visualization of all significant differences in this dataset multiple pairwise comparison test was performed in Python environment.

### | Figure 2

(A) Staining of F-actin (red) and  $\alpha$ -actinin-4 (green) and nuclei (blue on merged images) in MSCWJ-1. Cells were grown on glasses, fixed and permeabilised at passages 9, 15, 36. Polyclonal antibodies against human  $\alpha$ -actinin-4 and Alexa 488 secondary antibodies were used for  $\alpha$ -actinin-4 staining. Hoechst33342 was used for nuclei staining. Rhodamine

phalloidin was used to stain actin cytoskeleton.  $\alpha$ -actinin-4/F-actin (B) and  $\alpha$ -actinin-4/nucleus (C) colocalization in MSCWJ-1. Cells were grown on glasses, fixed and permeabilised at passages 9, 15, 28, 36. F-actin and  $\alpha$ -actinin-4 were stained as previously indicated. Ten fields of view were recorded using confocal microscopy, cells were manually selected on merged images and Kendall's colocalization coefficient (bTau) was measured in ImageJ, then data passed to R environment for statistical analysis. Boxplots shown over jitter plots. In jitter plots each point represents one observation. In boxplots horizontal lines indicate 1st quartile, mean 3d quartile, whiskers indicate range. Significant differences identified by the Wilcoxon test are shown as asterisks on square brackets (\*  $p < 0.05$ , \*\*\*  $p < 0.001$ , \*\*\*\*  $p < 0.0001$ , ns — not significant). Boxplots with means indicated by horizontal lines shown over jitter plots, each point indicate one observation. Kruskal-Wallis test p-values are indicated under each plot.

### Figure 3

(A) Cell stained with polyclonal antibodies against RhoA (green), rhodamine-phalloidin (red), and Hoechst33342 (blue). Cells were grown on glasses, fixed and permeabilised at passages 9, 15, 36. Polyclonal antibodies against synthetic peptide corresponding to amino acids 177-189 located near the C-terminus of human RhoA and Alexa 488 secondary antibodies were used for RhoA staining. Hoechst33342 was used for nuclei staining. Rhodamine phalloidin was used to stain actin cytoskeleton. RhoA/nucleus (B) and RhoA/F-actin (C) colocalization. MSCWJ-1 fixed at passages 9, 15, 28 and 36. RhoA/nucleus colocalization in MSCWJ-1. Cells were grown on glasses, fixed and permeabilised at passages 9, 15, 28, 36. RhoA and nuclei were stained as previously indicated. Ten fields of view were recorded using confocal microscopy, cells were manually selected on merged images and Kendall's colocalization coefficient (bTau) was measured in ImageJ, then data passed to R environment for statistical analysis. Boxplots shown over jitter plots. In jitter plots each point represents one observation. In boxplots horizontal lines indicate 1st quartile, mean 3d quartile, whiskers indicate range. Significant differences identified by the Wilcoxon test are shown as asterisks on square brackets (\*  $p < 0.05$ , \*\*\*  $p < 0.001$ , \*\*\*\*  $p < 0.0001$ , ns — not significant). Kruskal-Wallis test p-values are indicated under each plot.

### Figure 4

(A) Confocal view of RhoA in the nucleus. Cells were grown on glasses, fixed and permeabilised at passages 9, 15, 36. Polyclonal antibodies against synthetic peptide corresponding to amino acids 177-189 located near the C-terminus of human RhoA and Alexa 488 secondary antibodies were used for RhoA staining. Hoechst33342 was used for nuclei staining. Rhodamine phalloidin was used to stain actin cytoskeleton. One characteristic cell were selected and Z-scanning was performed to obtain 70 confocal sections, images were used to generate 3D models in LeicaX software, slices show sections passing through the nucleus. White scalebars equals to 10  $\mu\text{m}$  on image sections XY, XZ, YZ.

(B) Confocal view of myosin-9 and F-actin in cell lammella. Cells were grown on glasses, fixed and permeabilised at passage 36. Polyclonal antibodies against synthetic peptide corresponding to amino acids 1949-1960 of human nonmuscle myosin IIA and Alexa 488 secondary anti-rabbit antibodies were used for myosin-9 staining. Rhodamine phalloidin was used to stain actin cytoskeleton. One characteristic cell were selected.

(C) Confocal view of myosin-9 and F-actin in cell lammella. Cells were grown on glasses, fixed and permeabilised at passage 36. Polyclonal antibodies against synthetic peptide corresponding to amino acids 1949-1960 of human nonmuscle myosin IIA and Alexa 488 secondary anti-rabbit antibodies were used for myosin-9 staining. Rhodamine phalloidin was used to stain actin cytoskeleton. One characteristic cell were selected and Z-scanning was performed to obtain 50 confocal sections, images were used to generate 3D models in LeicaX software, slices show sections

passing through the lammella region. Scalebar equals to 5  $\mu\text{m}$  on image sections XY, XZ, YZ.

## Figure 5

Cell movement trajectory analysis. MSCWJ-1 cells were stained with Hoechst33342 and seeded in 6-well plate at passages 9, 15, 36. Then cells were incubated for 4 h for adhesion and the plate was transferred to CQ1 automated cytometer, where 40 fields of view were recorded within 24 hours from each well. Tracks were manually collected from recorded images in ImageJ and passed to R for further analysis. (A) Characteristic images from trajectory analysis workflow. (B) Statistical analysis of calculated trajectories. Boxplots shown over jitter plots. In jitter plots each point represents one observation. In boxplots horizontal lines indicate 1st quartile, mean, 3rd quartile, whiskers indicate range. Significant differences identified by the Wilcoxon test are shown as asterisks on square brackets (\*\* $p < 0.001$ , \*\*\* $p < 0.0001$ , ns — not significant). Kruskal-Wallis test  $p$ -values are indicated only where  $p > 0.00001$ .

## Figure 6

Gel chromatographic separation of cytoplasmic extracts from MSCWJ-1 at different stages of replicative senescence. MSCWJ-1 cells were grown in 10 dishes 10 cm in diameter and lysed at passages 9, 15, 28. Lysing was performed using an actin cytoskeleton preservation buffer as described in Experimental Procedures. Cytosolic extracts were loaded on Superose 6 column and 14 fractions (1 ml) were collected on ice during elution. Proteins were precipitated from the collected fractions and after sample preparation, electrophoretic separation was carried out in 12% acrilamide gels, then proteins were transferred to PVDF membranes and stained with primary and HRP-conjugated secondary antibodies. (A) Comparison of elution profiles from MSCWJ-1: blue line — passage 9, red line — passage 15, green line — passage 36. X axis indicates retention time, in minutes, Y axis indicates optical absorbance at 280 nm, in arbitrary units (a.u.). (B) Separation of a set of calibration proteins (blue line), Blue Dextran 2000 (green line) and acetone (red line). X axis indicates retention time, in minutes, Y axis indicates optical absorbance at 280 nm, in arbitrary units (a.u.). (C) Western blot detection of myosin-9,  $\alpha$ -actinin-4 and  $\beta$ -actin in fractions obtained as a result of gel-chromatographic separation of cytoplasmic extracts from WJMSC1 cells at passages 9, 15, 28. Polyclonal antibodies against synthetic peptide corresponding to amino acids 1949-1960 of human nonmuscle myosin IIA and monoclonal anti- $\beta$ -actin antibodies were used. Secondary HRP-conjugated antibodies were applied and visualized using ChemiDoc Touch system. Passages 9, 15, 28 denoted as p9, p15, p28. (D) Western blot detection of RhoA in fractions obtained as a result of gel-chromatographic separation of cytoplasmic extracts from WJMSC1 cells at passages 9, 15, 28. Polyclonal rabbit antibodies against synthetic peptide corresponding to amino acids 177-189 located near the C-terminus of human RhoA were used for RhoA staining. Secondary anti-rabbit HRP-conjugated antibodies were applied and visualized using ChemiDoc Touch system. Passages 9, 15, 28 denoted as p9, p15, p28.

## Tables

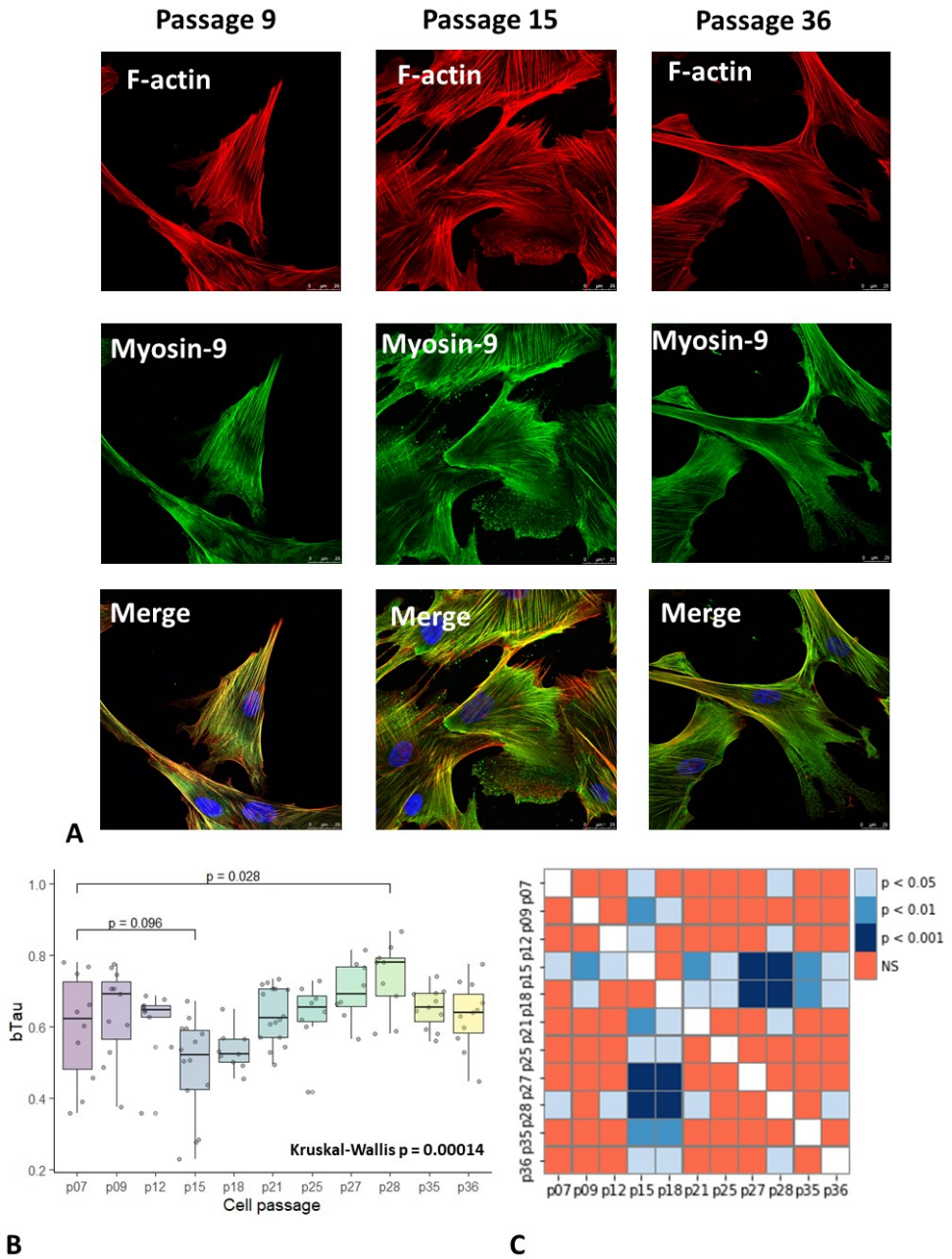
## Figures

**TABLE 1**  $\beta$ -galactosidase enzyme activity in MSCWJ-1 cells with limits of the 95% confidence intervals for binomial proportions. Cells were fixed and he number of cells stained for  $\beta$ -galactosidase was counted using light microscopy.

Passage Number	Cells stained, %	Cell count
9	$6.02 \pm 0.72$	3724
15	$20.55 \pm 1.57$	2404
28	$25.56 \pm 2.72$	1260
36	$37.62 \pm 2.91$	1026

**TABLE 2** MSCWJ-1 24 h movement trajectory analysis. Cells were stained with Hoechst33342 and seeded in 6-well plate at passages 9, 15, 36. From each well 40 fields of view were recorded within 24 hours on CQ1 automated cytometer, then tracks were manually collected from recorded images in ImageJ and passed to R for further analysis. Mean  $\pm$  SD shown for calculated movement parameters.

Passage	Track count	Mean Speed, $\mu\text{m/h}$	Max Speed, $\mu\text{m/h}$	Length, $\mu\text{m}$	Distance, $\mu\text{m}$
9	171	$38.3 \pm 15.2$	$164.9 \pm 56.4$	$911.3 \pm 362.4$	$278.2 \pm 169.8$
15	172	$25.0 \pm 11.1$	$127.9 \pm 59.3$	$595.1 \pm 263.4$	$211.7 \pm 162.8$
36	178	$18.3 \pm 7.7$	$57.1 \pm 27.8$	$431.6 \pm 174.5$	$215.1 \pm 156.4$



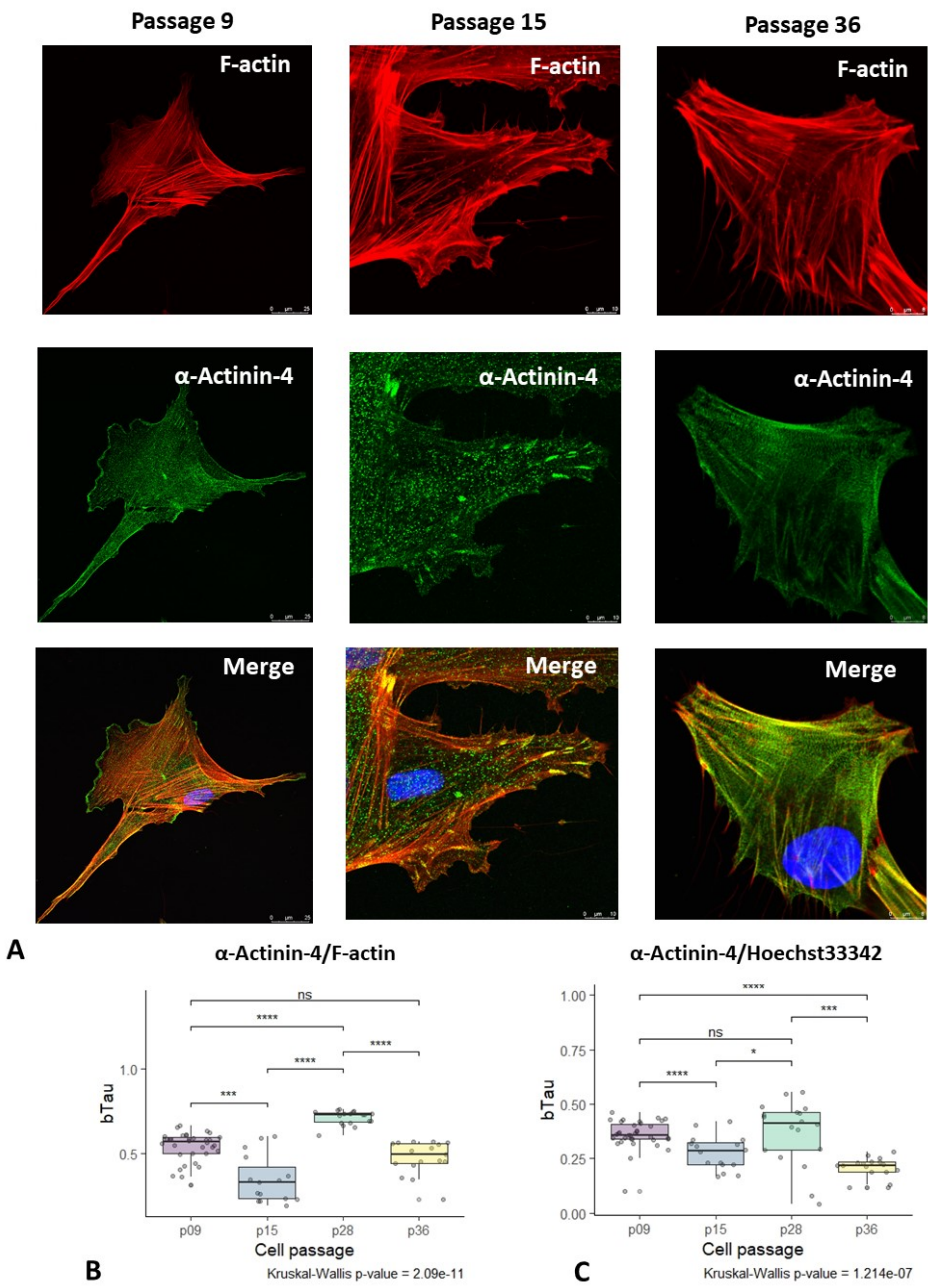


FIGURE 2

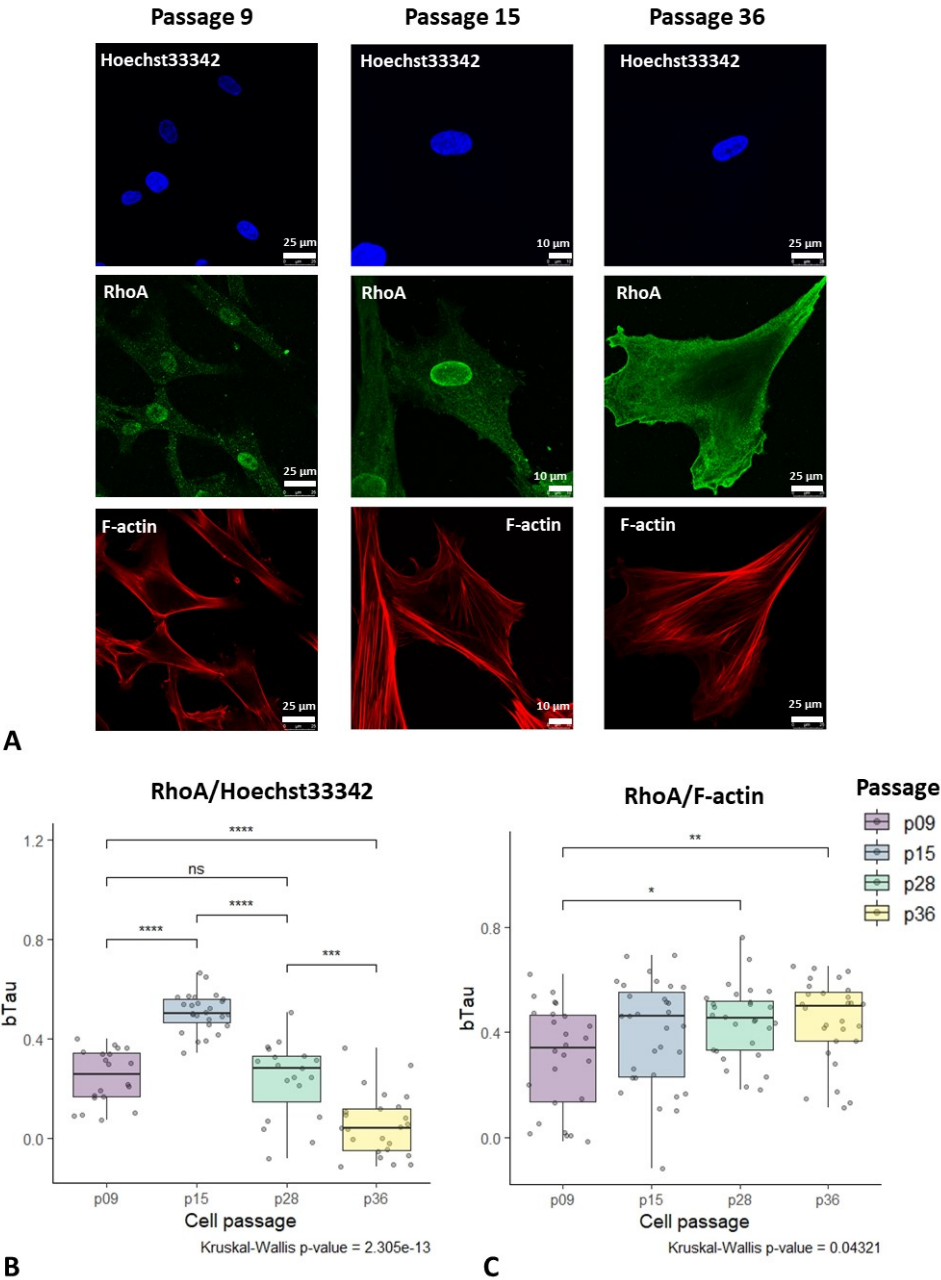


FIGURE 3

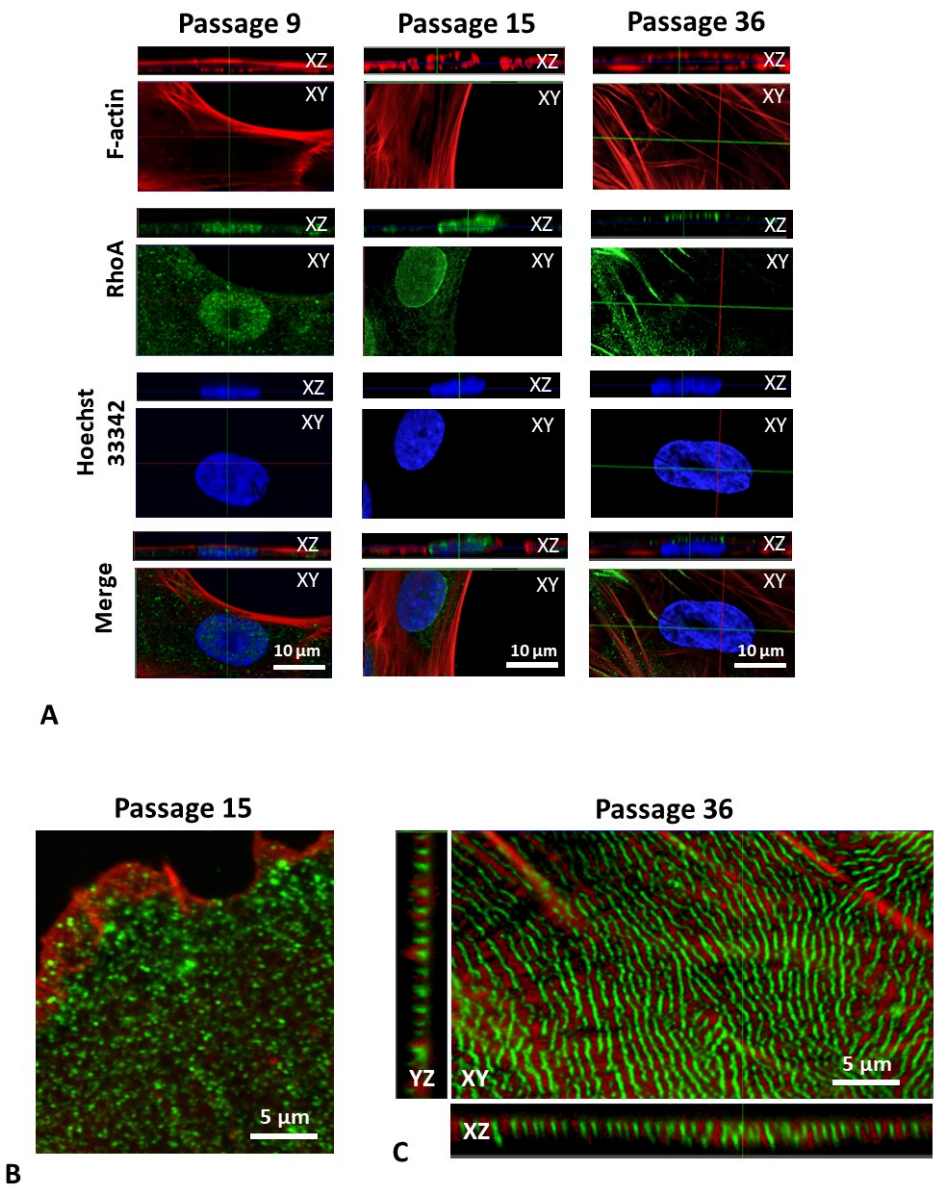


FIGURE 4



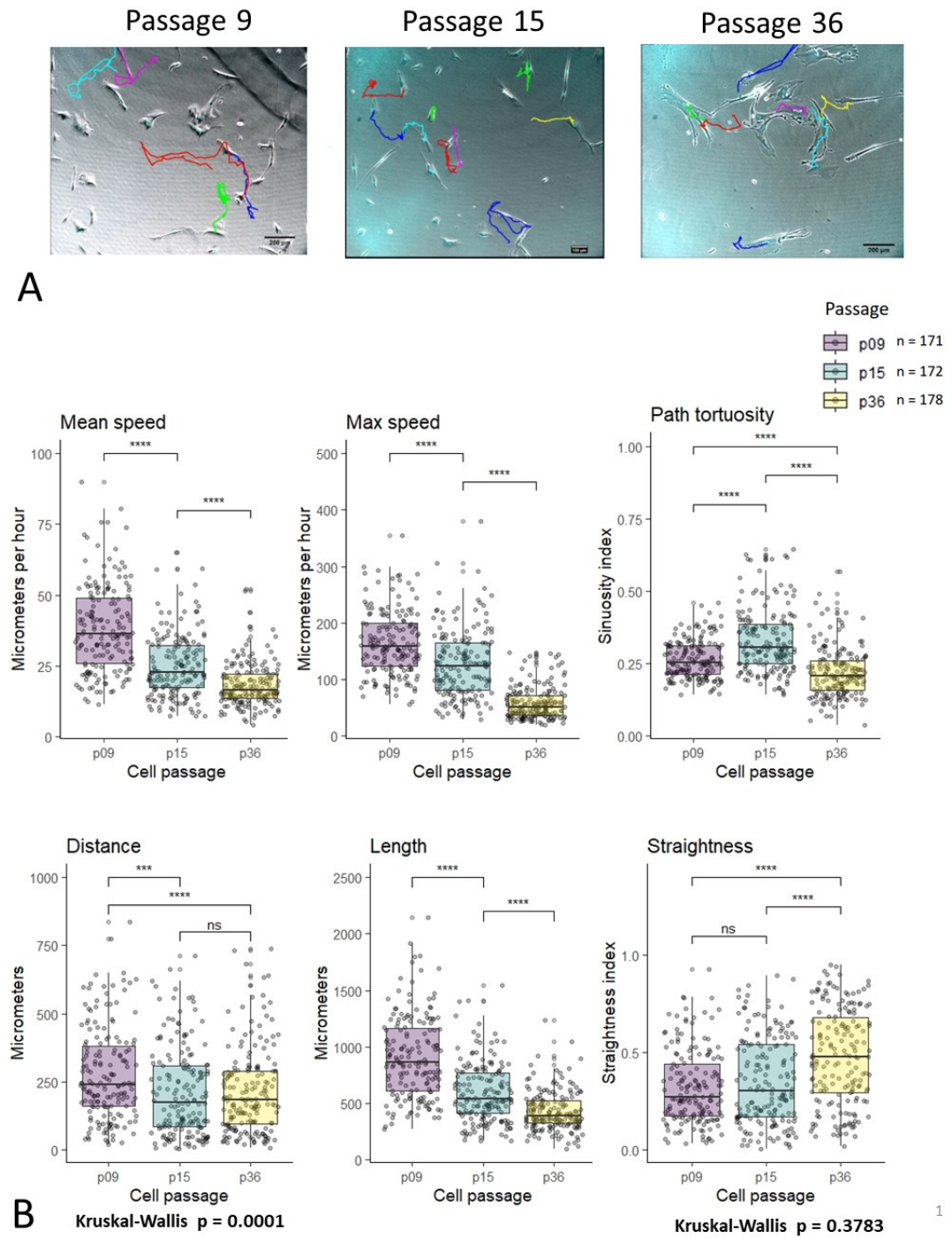


FIGURE 5

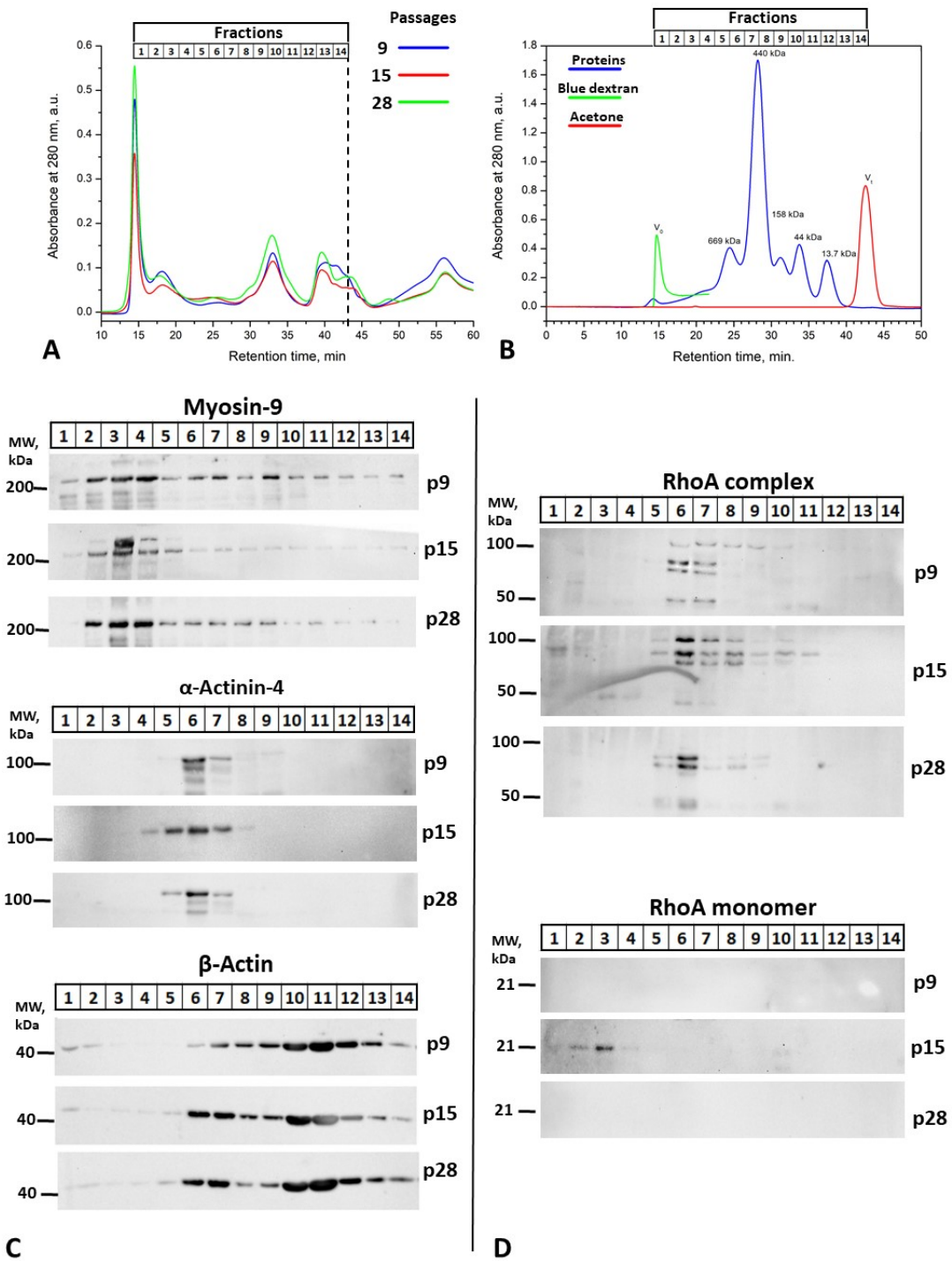


FIGURE 6